SANDIA REPORT

SAND96–1933 • UC–706
Unlimited Release
Printed August 1996

Feasibility Study of Parallel Optical Correlation-Decoding Analysis of Lightning

Michael R. Descour, William C. Sweatt, Glenn R. Elliott ,
Mark L. Yee, Richard E. Spalding

Prepared by
Sandia National Laboratories
Albuquerque, New Mexico 87185 and Livermore, California 94550
for the United States Department of Energy
under Contract DE-AC04-94AL85000

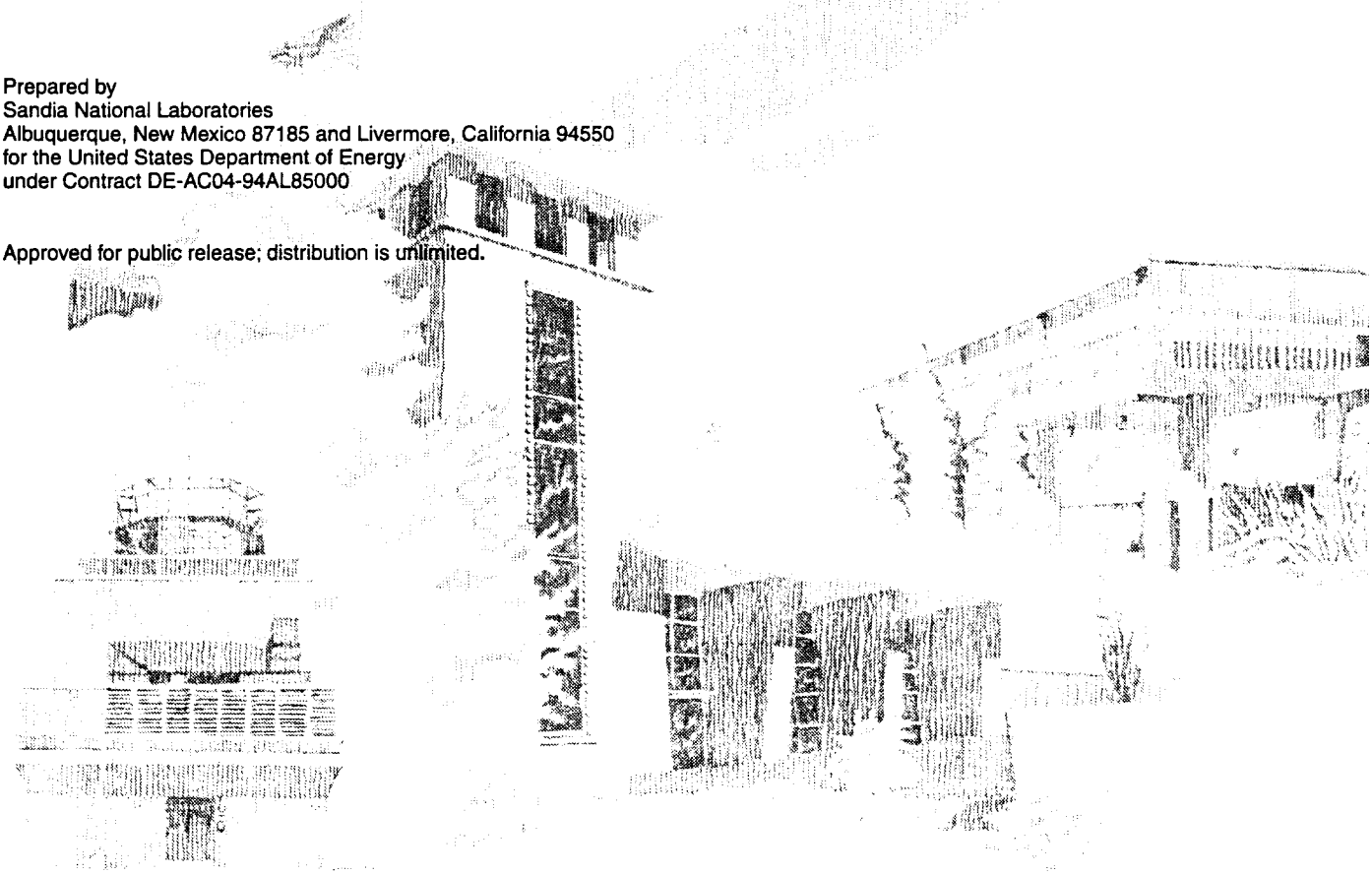

SF2900Q(8-81)

Issued by Sandia National Laboratories, operated for the United States Department of Energy by Sandia Corporation.

Available to DOE and DOE contractors from
Office of Scientific and Technical Information
P.O. Box 62
Oak Ridge, TN 37831

Prices available from (615) 576-8401, FTS 626-8401

Available to the public from
National Technical Information Service
U.S. Department of Commerce
5285 Port Royal Rd
Springfield, VA 22161

NTIS price codes
Printed copy: A04
Microfiche copy: A01

SAND96-1933
Unlimited Release
Printed August 1996

Distribution
Category UC-706

Feasibility study of parallel optical correlation-decoding analysis of lightning

Michael R. Descour,† William C. Sweatt, and Glenn R. Elliott
Optics and Exploratory Technologies

Mark L. Yee
Exploratory Image Processing Systems Department II

Richard E. Spalding
Senior Engineer for Exploratory Technology

Sandia National Laboratories
Albuquerque, New Mexico 87185

†Optical Sciences Center
University of Arizona
Tucson, Arizona 85721

Abstract

The optical correlator described in this report is intended to serve as an attention-focusing processor. The objective is to narrowly bracket the range of a parameter value that characterizes the correlator input. The input is a waveform collected by a satellite-borne receiver. In the correlator, this waveform is simultaneously correlated with an ensemble of ionosphere impulse-response functions, each corresponding to a different total-electron-count (TEC) value. We have found that correlation is an effective method of bracketing the range of TEC values likely to be represented by the input waveform. High accuracy in a computational sense is not required of the correlator. Binarization of the impulse-response functions and the input waveforms prior to correlation results in a lower correlation-peak-to-background-fluctuation (signal-to-noise) ratio than the peak that is obtained when all waveforms retain their grayscale values. The results presented in this report were obtained by means of an acousto-optic correlator previously developed at SNL as well as by simulation. An optical-processor architecture optimized for 1D correlation of long waveforms characteristic of this application is described. Discussions of correlator components, such as optics, acousto-optic cells, digital micromirror devices, laser diodes, and VCSELs are included.

Nomenclature

1D	one dimensional
2D	two dimensional
AO	acousto-optic
CCD	charge-coupled device
CW	continuous wave
DAC	digital-to-analog converter
IRF	impulse-response function
LED	light-emitting diode
L-I	light-current relationship
TEC	total electron count, measured in 10^{17} electrons/m^2
CP_{env}	correlation peak, envelope
CP_{pos}	correlation peak, positive maximum

Contents

Figures

Feasibility Study of Parallel Optical Correlation-decoding for Analysis of Lightning

Introduction

The optical processor decodes electromagnetic data that has been dispersed by the ionosphere between the data's origin and a satellite. The exact origin of the signal on earth is unknown and so the dispersing function is also unknown. Therefore, the signal is decoded with several impulse-response functions (IRFs) that represent different total electron counts (TECs). For a given quantity of free electrons in the ionosphere, different TEC values correspond to different path-lengths through the ionosphere. Fluctuations in the number of free electrons in the ionosphere are caused by Sun spot activity, for example. The number also varies with time-of-day (higher during the day than at night).

The electromagnetic sources of interest tend to radiate groups of Dirac-delta functions distributed in time. Lightning is an example of this type of source. When the dispersed signal is correlation-decoded with the correct IRF, the result is a sequence of "bright" peaks. Subsequently, an intensity discriminator can be used to locate these peaks in the background fluctuations.

Correlation-decoding and Matched-filtering

Both terms may refer to the same operation. Matched-filtering is different from correlation-decoding when the two functions to be correlated undergo different preprocessing; for example, the kernel may be binarized but not so the input waveform. In the case of this report, both the kernel and the input waveform are treated identically and so we will use the terms *correlation-decoding* or just *correlation* and matched-filtering as synonyms.

The task addressed in this report is one of detection of a known signal or signals. Consequently, high computational accuracy is not required. A major limitation of optical processors is thereby eliminated. At its simplest, a matched-filter processor detects the presence of a pattern in an input by correlating the input data with the pattern. As an example, consider the detection of a tank in a two-dimensional reconnaissance image. The problem described in this report consists of determining which of an *ensemble* of patterns is present in an input and where it is present. This is equivalent to simultaneously detecting a tank, a truck, and an aircraft in an input scene. The choice of the right or *optimal* pattern is based on the characteristics of the correlation peak(s) that each pattern causes. In brief, the more a correlation peak resembles the Dirac-delta-function-like signal spike, the more optimal the selected pattern.

Objectives

The identification of a pair of most optimal IRFs brackets the likely range of TEC values encountered by the collected signal. This is the meaning of *attention-focusing*. Subsequent constrained (and most likely digital) analysis of the input signal can reveal

the time of the generating event (lightning strike) and a range of likely origin locations. Analysis of similar data from differently positioned sensors can further constrain the origin of the event.

The goal of our work was to examine the problem of lightning-strike analysis by means of an existing optical correlator designed and built at Sandia National Laboratories. Specifically, the variation of the correlation peak with TEC was examined in simulation on a computer and in experiment by using the Sandia correlator. The results were then related to the background fluctuations in the correlation-decoded outputs. This background fluctuation is related to noise in the input waveforms and, in the case of the correlator, noise associated with the optical processor itself. Noise in the correlator originates in the LED sources, the AO cell, and the CCD array.

Experimental Implementation

The platform for the experimental work is a time-integrating, 2D AO correlator developed at Sandia National Laboratories by Stalker, *et al.*[1] This correlator traces its heritage to the work by Sprague and Koliopoulos[2] and more recently directly to the efforts of Psaltis.[3]

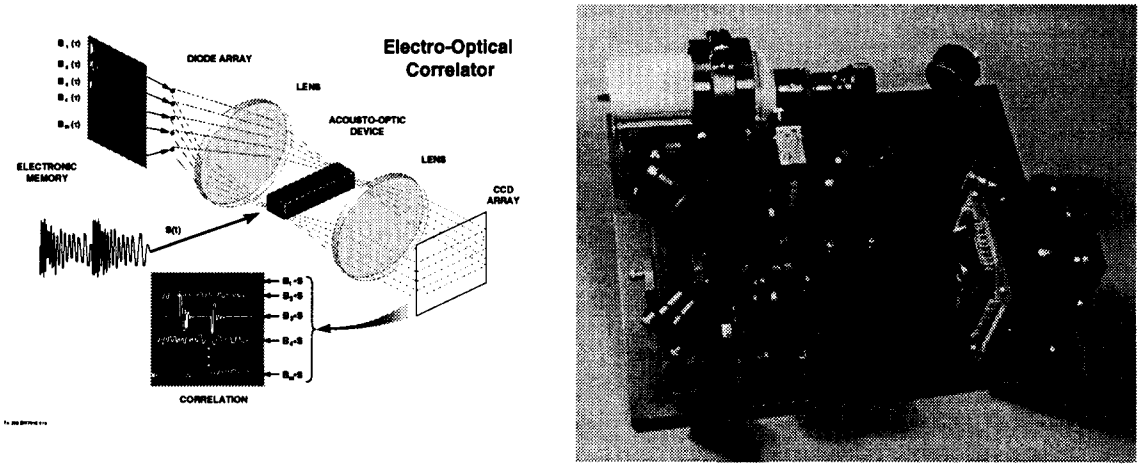

(a) (b)

Figure 1. Layout of the Sandia AO correlator. A schematic of the correlator is shown in (a). The actual layout of the hardware is shown in (b). See text for description.

The Sandia correlator (see Fig. 1) suited our needs because it is based on components likely to be incorporated into a specialized, ionosphere IRF processing instrument. Specifically, the impulse response is emitted by an array of LEDs (lower right in Fig. 1), the input waveform is introduced via an AO tellurium dioxide (TeO_2) Bragg cell (center) and the results are sensed by a CCD camera (upper left).

The Sandia correlator also imposes certain constraints. First and foremost, it is a 2D correlator. The correlator can be converted for operation with 1D inputs by modifying the computer control software. We found it more expedient to encode the 1D impulse responses and waveforms into 2D patterns in order to be compatible with the correlator's nominal operation. In addition, the low radiance and relatively slow temporal response of the correlator's LED sources (as compared to alternative sources, such as laser diodes) requires the binarization and oversampling of the input signals.

The properties of the TeO_2 cell are summarized in the table below.

Property	Specification
acoustic velocity, v	617 m/s
time window	40 ms
carrier frequency	50 MHz
time-bandwidth product	2000

Binarization and Offset

Binarization is equivalent to the *signum* function,

$$sign(x) = \begin{cases} 0, & x = 0 \\ 1, & x > 0 \\ -1, & x < 0 \end{cases}. \tag{1}$$

The function's application to an IRF increases the average radiance associated with the impulse response as generated by the LED array. Binarization also increases the average diffraction efficiency associated with the input waveform in the Bragg cell.

The input waveform as well as the ensemble of IRFs consist of data that can take on negative as well as positive values. This presents a problem since the sources in the correlator can only emit nonnegative amounts of light and the amplitude modulation of the carrier frequency imparted to the AO cell suffers the same limitation. A bias can be added to the two correlator inputs to solve this problem but this leads to a large DC offset in the correlation results.[3,4] Our solution is to break up the problem into several component correlations whose outputs are later electronically combined to yield the desired result.

We treat a signal (waveform or impulse response), $s(t)$, as a sum of a positive part, s_+, and a negative part, s_-,

$$s(t) = s_+(t) - s_-(t). \tag{2}$$

Note that the choice of sign indicates that both s_+ and s_- are nonnegative functions of time and thus compatible with the LEDs and the AO-cell diffraction efficiency. Next, the correlation of the input waveform, $r(t)$, with an input impulse-response function, $h(t)$, can be expanded to read

$$r(t) \star h(t) = [r_+ - r_-] \star [h_+ - h_-] = r_+ \star h_+ - r_+ \star h_- - r_- \star h_+ + r_- \star h_-, \qquad (3)$$

where the symbol, $\star$, indicates correlation.

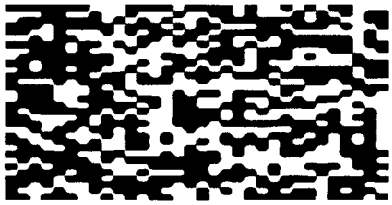

Figure 2. An example 2D-encoded impulse response.

Two-dimensional Encoding of the Input Signals

In order to be compatible with the Sandia correlator, the 1D input signals must become 2D input patterns. This step introduces a large amount of overhead and makes the correlator very inefficient. Out of each output 512×240-pixel image, only 108 pixels are extracted with relevant correlation results. This means an efficiency of 0.087%. This efficiency must be viewed in context. The Sandia correlator is only being used as an experimental platform to evaluate optical correlation applied to ionosphere impulse responses. A correlator architecture optimized for 1D inputs will have a 100% efficiency according to the above convention.

Figure 2 shows an example of an encoded impulse response. The pattern shown measures 64×32 pixels as dictated by the configuration of the Sandia correlator. Note that the bright and dark pixels occur in pairs in the horizontal direction. This is a result of the previously mentioned oversampling of the impulse response and input waveform dictated by the relatively slow temporal response of the LED sources.

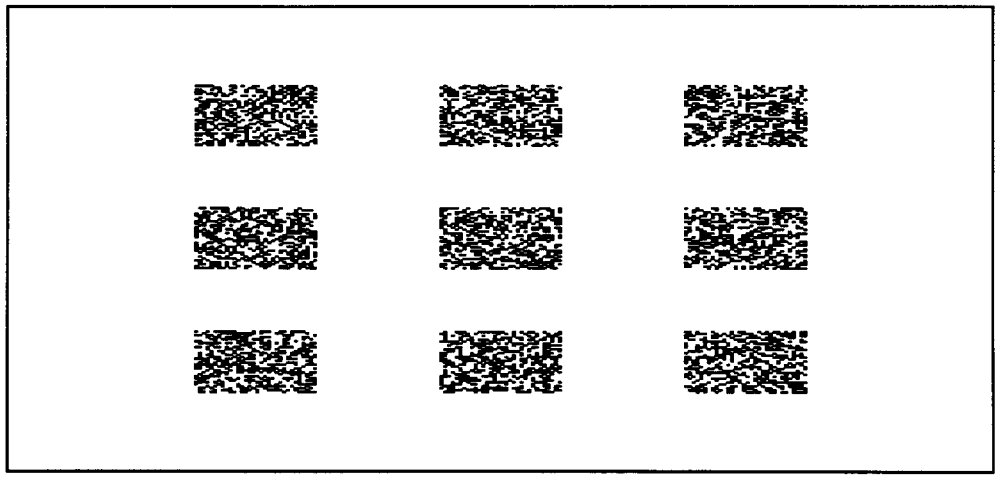

Figure 3. An example of an input image used to modulate the AO cell. Each of the nine patterns represents a 1024-sample long window along the 1D input waveform.

Figure 3 shows an example of a 512×240 input image. Row after row of this image is used to amplitude-modulate the carrier frequency driving the AO cell.[1] Each of the nine patterns shown in the Figure represents a 1024-sample long window along the input waveform. As we proceed from one pattern to the next in raster fashion, each pattern encountered represents a shift of the window by one sample along the waveform. Any given input image then contains data from nine consecutive positions of the 1024-sample long window.

Results

The Basic Algorithm

Figure 4 illustrates an input waveform. This particular example is based on a model and represents the result of ionosphere dispersion and white noise on a pair of Dirac-delta-function pulses occurring in quick succession.[5]

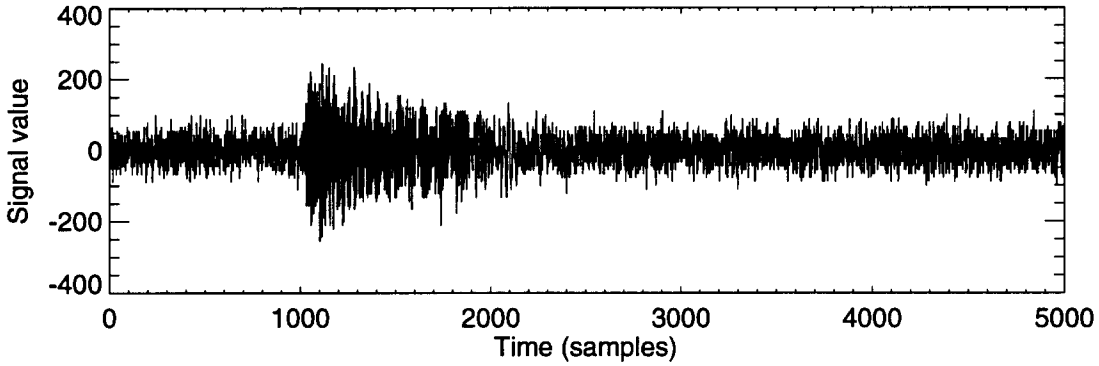

Figure 4. Example input waveform.

The data shown in Fig. 4 are next correlated with an ensemble of IRFs, each corresponding to a different TEC value. We anticipate a nominal value of 20 IRFs being needed for this application. Shown in Figure 5 is the optimal IRF, associated with a TEC value of 1.1.

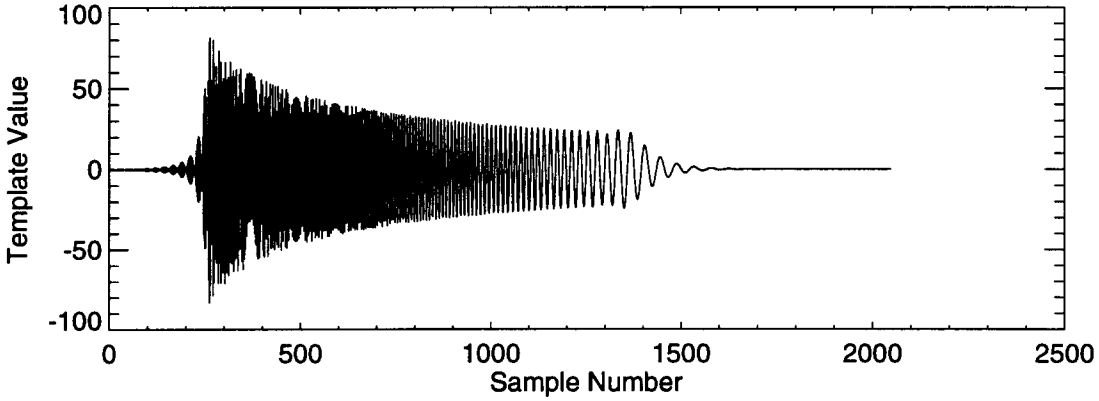

Figure 5. Example ionosphere IRF. This particular response is characteristic of a TEC = 1.1.

Figure 6 illustrates the result of correlation-decoding the data in Fig. 4 with the IRF in Fig. 5. The two peaks around the 800th sample clearly stand out above the background fluctuations. The result shown in Fig. 6 was obtained experimentally, i.e. using the Sandia correlator, after the input waveform and the IRF were binarized according to Eq. (1).

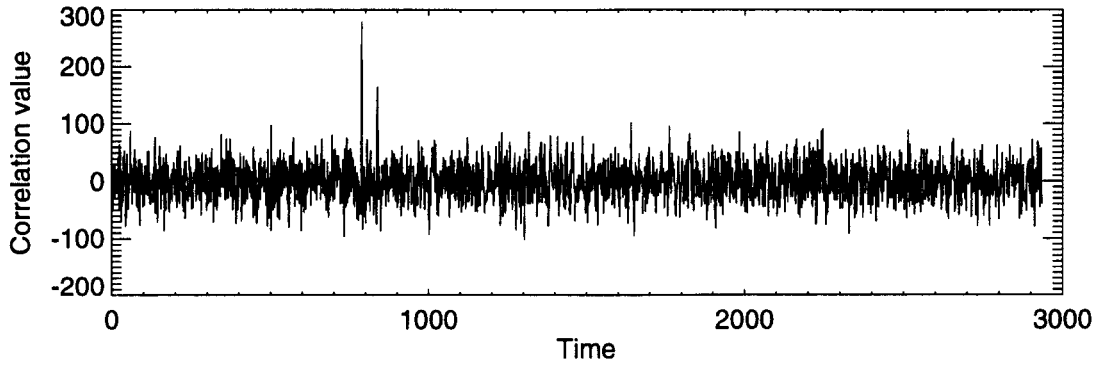

Figure 6. The output of the optical processor. In this case, the correct IRF with TEC = 1.1 was used on the input waveform. The input waveform and the IRF were binarized prior to correlation.

Correlation with an incorrect IRF, i.e. the wrong value of the TEC, does not result in a pronounced, Dirac-delta-function-like peak or series of peaks. Figure 7 illustrates this effect. This result was also obtained using the Sandia correlator after both the input waveform and the IRF were binarized.

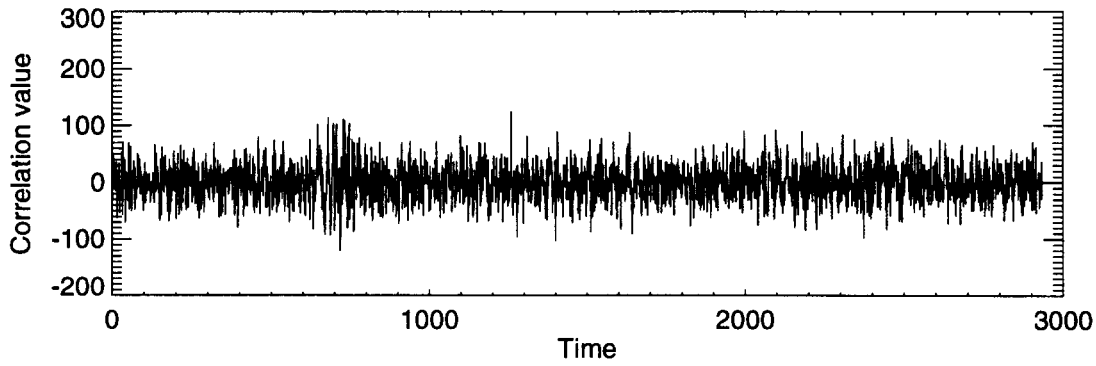

Figure 7. The output of the optical processor due to an incorrect TEC-value IRF.

Figures 6 and 7 provide an example of the difference between correlation with an optimal and an incorrect IRF. Next, this analysis is extended to determine how precisely correlation-decoding can identify the right TEC value under a variety of conditions.

Correlation Peak (*CP*) vs. Total Electron Count

The table below shows the options examined in this report. Subsequent figures illustrate simulation results associated with the four combinations. Experimentally, only white-noise/binarized-waveform-and-IRF results are available. Table 1 provides a roadmap to the locations of the results generated for this report.

Binarization/Grayscale	Simulated/Experimental Correlation	Noise	Figure
grayscale	simulated	white	9
binarization	simulated	white	10
grayscale	experimental	white	N/A
binarization	experimental	white	11
grayscale	simulated	white noise only	14
binarization	simulated	white noise only	15
grayscale	simulated	white noise and CW interference	16
binarization	simulated	white noise and CW interference	17

Table 1. Listing of CP_{env} vs. TEC plots.

The input waveform shown in Fig. 4 was correlation decoded with IRFs associated with TEC values ranging from 0.8 to 1.6. The maximum correlation peak was expected at TEC = 1.1.

The event we are reconstructing consisted of two pulses (see Fig. 6). In order to evaluate the peak vs. TEC-value behavior, we chose to use the first pulse as reference.

Correlation peaks were defined as the maximum signal in the correlation-decoded data. Results subject to two slightly different correlation-peak definitions are shown in Figs. 9-12. The *envelope* peak was defined as

$$CP_{env}(TEC) = \max\left[\left| r(t) \star h(t, TEC) \right|\right] \tag{4}$$

and the *positive* peak was defined as

$$CP_{pos}(TEC) = \max\left[r(t) \star h(t, TEC)\right]. \tag{5}$$

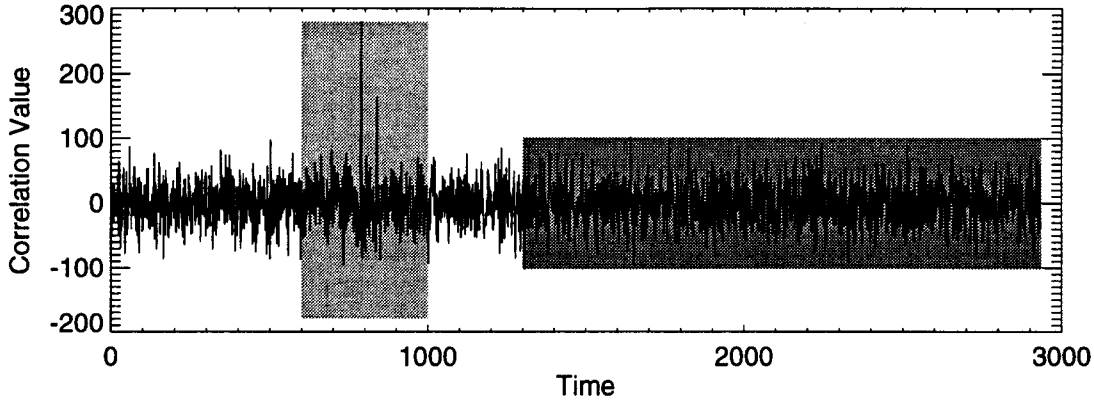

Figure 8. Relevant sections of the correlation decoded data. Correlation peaks occurred in the section of the data highlighted by light gray. Data in the dark-gray section were used to compute the variance of the "background" in the processed data.

Analysis results were based on waveform sections highlighted in Fig. 8. For the indicated range of TEC values, [0.8, 1.6], the correlation peak occurred in the section highlighted in lighter gray, irrespective of peak definition [Eqs. (4) and (5)]. The peak values illustrated in the plots below were therefore taken from this region after correlation of the input waveform with an IRF. The corresponding level of background fluctuation was calculated based on the samples contained within the section highlighted in darker gray.

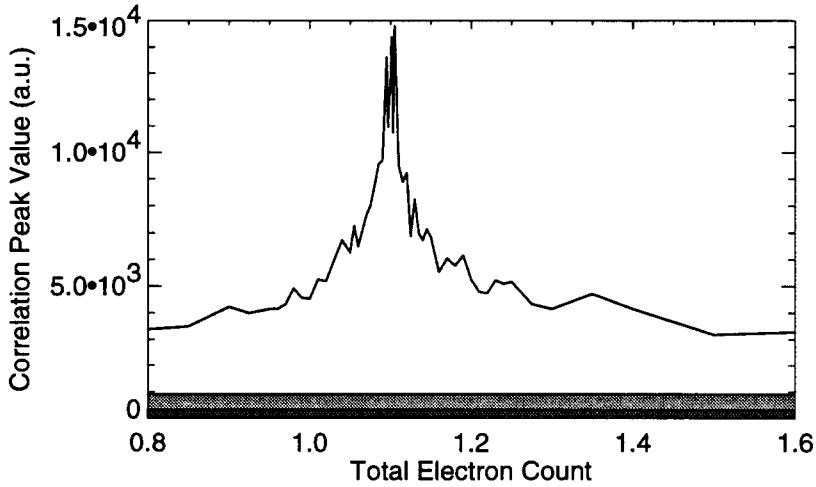

Figure 9. Simulated CP_{env} variation with TEC value: grayscale case.

Figure 9 shows the result for the simulated white-noise/grayscale case. In this case, the waveform data and the IRFs retained their grayscale values. The two curves shaded in gray at the bottom of the plot indicate the variation of the "background" in the correlation-decoded data (see Fig. 8). The darker-gray band corresponds to $+\sigma$ and the lighter gray band is indicative of $+3\sigma$. The units on the ordinate axis are arbitrary, hence *a.u.* The correlation-peak curve shown in Fig. 9 was obtained by simulation. A TEC value of 1.1 results in a high envelope peak value but the peak is not unique. Correlation peaks also occur at TEC = 1.105 and TEC = 1.095. The maximum peak, in fact, is associated with TEC = 1.105. However, from the perspective of an attention-focusing optical preprocessor, these ambiguities are not a problem. Within the context of Fig. 9, the preprocessor's function would have been fulfilled by simply locating the peak in the range [1, 1.2]. Subsequent analysis would then be performed to identify a more accurate TEC value.

Binarization of the input waveform and the IRF decreases the correlation-peak-to-background-fluctuation ratio in the presence of white noise, as illustrated in Fig. 10. Note that the noise level increases with increasing TEC value. This appears to be generally true when the waveform and IRF are binarized. Larger TEC values correspond to temporally longer IRFs. Each point along the correlation-decoded waveform corresponds to a summation of weighted random variables (independent and identically distributed, in the case of white noise). The longer the IRF, the more equally-weighted terms in the sum and thus the greater the background fluctuation at larger TEC values.

On the other hand, the background fluctuation does not exhibit a similarly pronounced growing trend with increasing TEC in the case of grayscale inputs (see Fig. 9). Grayscale IRFs retain an envelope that decays in time (see Fig. 5). As in the binarized case, the longer the IRF the more terms in the summation that yields a point along the correlation-decoded waveform. Due to the decaying envelope, terms corresponding to later sections of the IRF make a weaker contribution to the summation result than those terms occurring earlier in the IRF. The effect of a longer-duration IRF on the background-fluctuation level is therefore not as pronounced as it is in the binarized case where all terms receive equal weighting, as described by Eq. (1).

The optical correlator processed only binarized data and the correlation-peak vs. TEC variation was only evaluated in the case of a white-noise corrupted waveform. The processor contributes about 11% of the total variance illustrated in Fig. 11. The processor's contribution was evaluated by repeatedly recording the correlation peak value associated with TEC = 1.1 and then computing the statistics of the collected data. The resulting standard deviation was found to be 10.7 units on the scale used in Fig. 11.

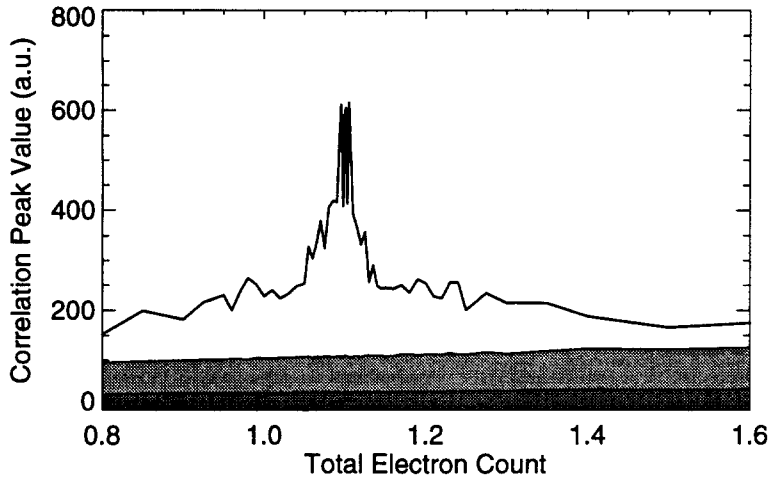

Figure 10. Simulated CP_{env} variation with TEC value: binarized case.

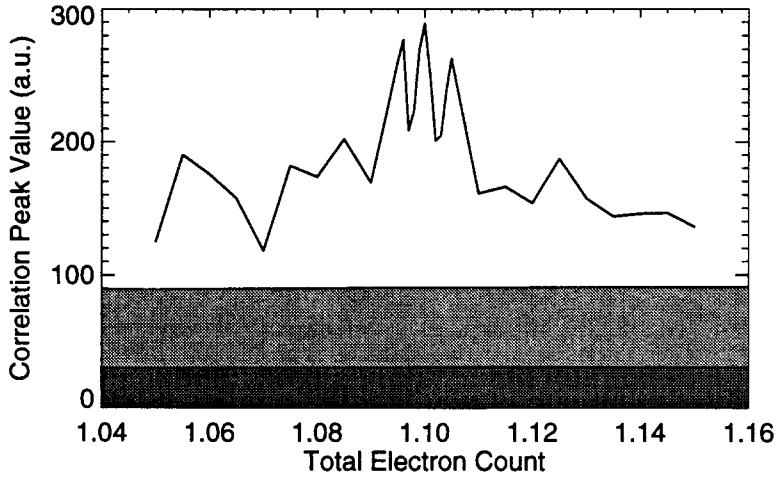

Figure 11. Experimentally derived CP_{env} variation with TEC. The meaning of the gray-shaded curves is the same as in Figs. 9-10. Note that this plot's abscissa encompasses only the near-optimal TEC-value region.

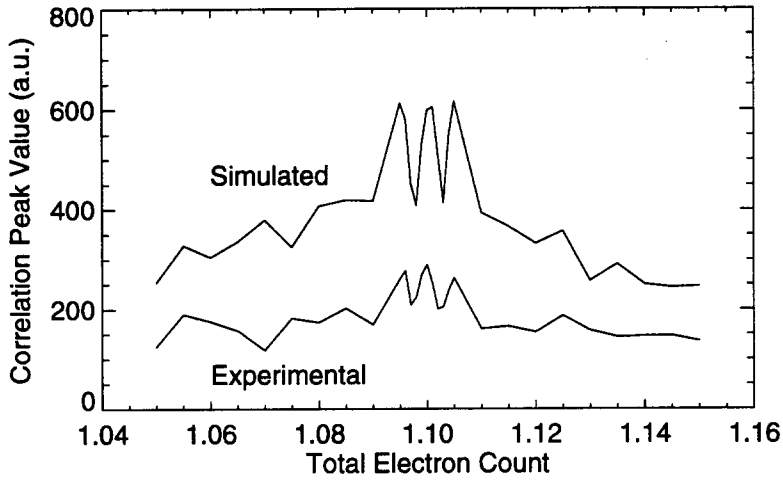

Figure 12. Comparison of simulated and experimental CP_{env} variation with TEC. This plot highlights the similarity between the simulated and experimental results around the optimal TEC value of 1.1.

Comparison between Simulated and Experimental Correlation Results

As a consistency check, the correlation-peak vs. TEC results were compared for the simulated and experimental cases. Figures 12 and 13 illustrate the results of this comparison and the similarity observed between the two cases. Figure 12 is based on the envelope-peak definition of Eq. (4) and Figure 13 is based on the positive-peak definition in Eq. (5).

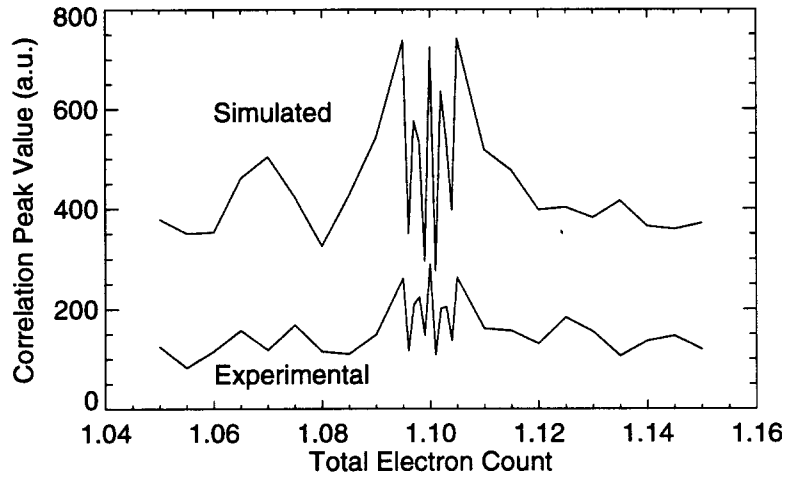

Figure 13. Simulated and experimental CP_{pos} value vs. TEC. This plot offers a different perspective [see Eq. (5)] on the results shown in Figs. 9-12. Experimental results closely resemble the simulated outcomes.

Introduction of an Interfering CW signal

All the simulation and experimental results presented up to this point used input waveform data corrupted with additive white noise only. By means of simulation, we also examined the effects of the introduction of an interfering CW signal, such as a radio transmitter. The CW signal was introduced in addition to white noise. Figures 14-15 present white-noise-only results. Figure 14 illustrates the correlation results when grayscale information is retained in the waveform and the IRFs. Figure 15 shows the result of binarization of both the waveform and the IRFs.

The addition of a CW signal results in correlation-peak plots shown in Figure 16 for the grayscale case and Figure 17 for the binarized case.

In the grayscale case, introduction of a CW signal affects the background-fluctuation level but has little effect on the maximum correlation-peak values (compare Figs. 14 and 16). The correlation-peak-to-background ratio decreases. In the binarized case, the correlation-peak-to-background ratio decreases as well but primarily because of a drop in the maximum correlation-peak value (compare Figs. 15 and 17). The fluctuation level appears to remain approximately the same, although some oscillations appear.

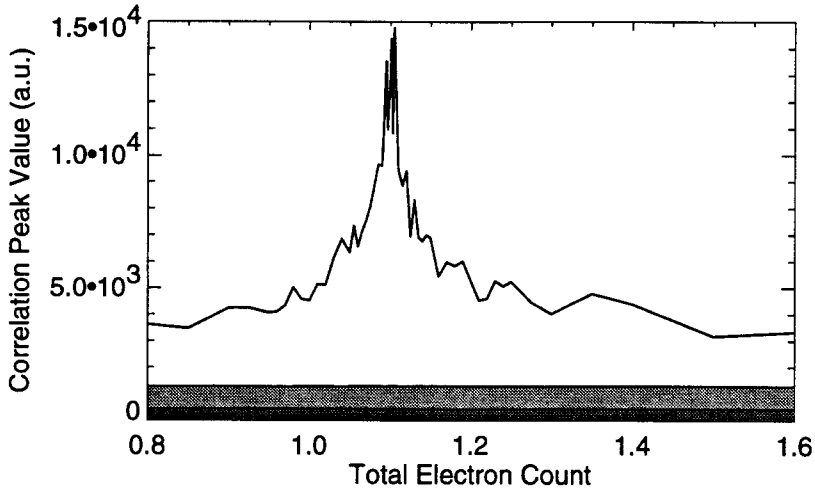

Figure 14. Simulated CP_{env} variation with TEC for an input waveform corrupted only by additive white noise: grayscale case.

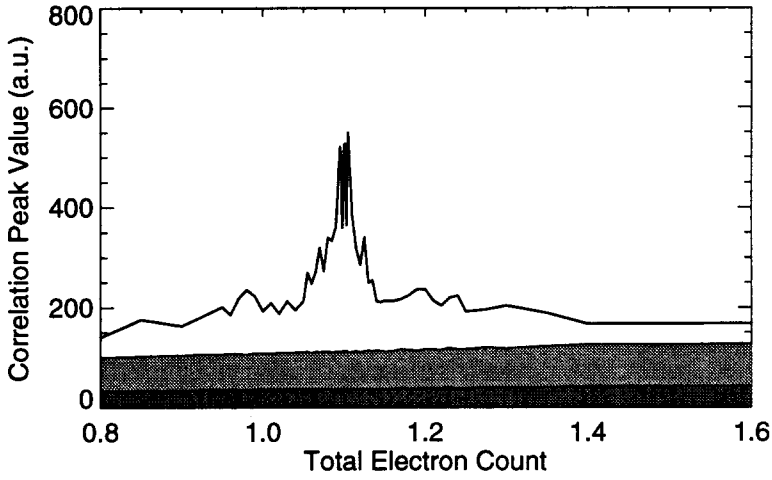

Figure 15. Simulated CP_{env} variation with TEC for an input waveform corrupted only by additive white noise: binarized case.

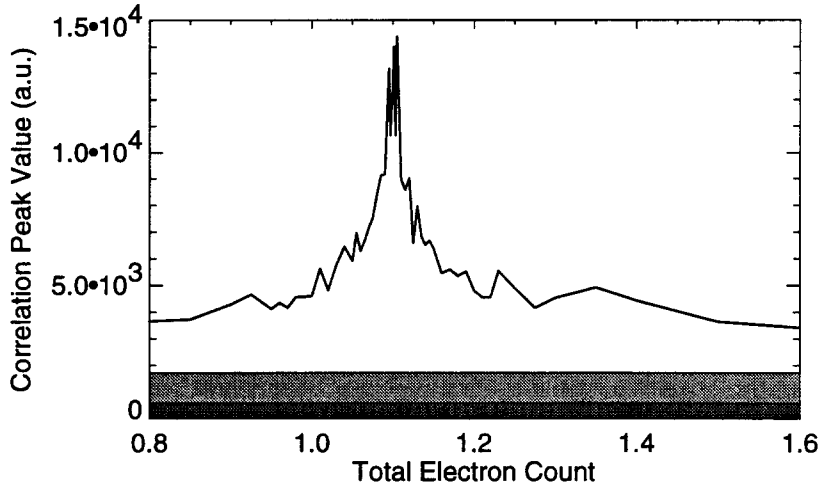

Figure 16. Simulated CP_{env} variation with TEC for an input waveform corrupted by a CW signal: grayscale case.

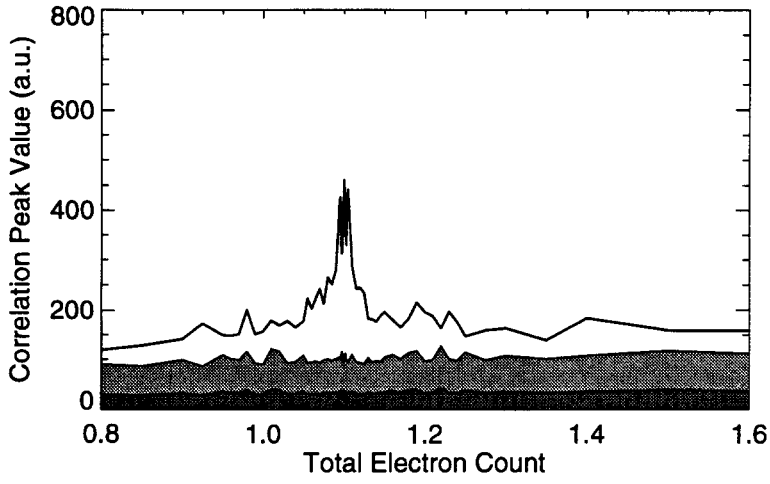

Figure 17. Simulated CP_{env} variation with TEC for an input waveform corrupted by a CW signal: binarized case.

Architectural Features

The input signal is assumed to have a 10-MHz bandwidth. Consequently, a CCD with 512-pixel rows can store 25.6 microseconds (μs) of data per row at Nyquist sampling. If 18 IRFs are needed to sufficiently divide the full TEC-value range of interest then 36 rows are required per each 25.6-μs block of data [recall Eq. (2)]. Fourteen (14) of these blocks can be fit on a 512×512-pixel CCD, so the total record will be 358.4 μs per frame.

Figure 18 shows the data flow through the system with time plotted on the horizontal axis and CCD-row number on the vertical axis. The top line shows the positive part of the input waveform, r_+, on the left side and the negative part, r_-, on the right side (later in time). In the upper left quadrant of the Figure there are 14 blocks of IRFs. The top block of 18 diodes begin flashing h_+ when the beginning of the waveform r_+ reaches the end of the AO cell. Recorded in the first block is a correlation-decoded version of the positive part of any signal that actually occurred during the first 25.6 microseconds. The IRFs in the second block are identical to those in the first block except that they are delayed by 25.6 μs. Thus events that occurred between 25.6 μs and 51.2 μs are recorded there. Events occurring between 51.2 μs and 76.8 μs will be recorded in the fourth block and so on. During 358.4 μs, $r_+ \star h_+$ is recorded in the 14 blocks in the upper left quadrant.

During the first half of a frame time, the positive signal component, r_+, flows across the AO cell. During the second half of a frame time, the negative component, r_-, is fed through the AO cell. The upper-right quadrant of the Figure indicates that the diodes are modulated by the negative components of the IRFs. This produces the

correlation $r_- \star h_-$ and adds it to the correlation $r_+ \star h_+$ described in the previous paragraph. As above, the second block is the same as the first except that it is delayed by 25.6 μs, the third block is delayed by 51.2 μs, the fourth block is delayed by 76.8 μs, and so on. At the end of the frame time, half of the total correlation will have been computed in the upper half of the CCD,

$$f_{pos} = r_+ \star h_+ + r_- \star h_- . \tag{6}$$

The lower half of Fig. 18 is identical to the top except that the negative and positive components, h_- and h_+, have been interchanged. Therefore the cross correlations are computed, resulting in the other half of the total correlation,

$$f_{neg} = r_+ \star h_- + r_- \star h_+ . \tag{7}$$

If the bottom half of the CCD frame is subtracted from the top half, the desired correlation is achieved,

$$r \star h = f_{pos} - f_{neg} . \tag{8}$$

Note that the dispersed signal from an electromagnetic event can be spread out over tens of microseconds by an IRF. Therefore, the correlation being attempted by the optical correlator can proceed for a long time. This architecture for a 10-MHz signal and 14 blocks of 18 IRFs allows each IRF to be 75 μs long if the CCD frame rate is 1,000 Hz. The IRF duration is computed from the following: half the frame time is 500 μs, the 14 blocks are 358 μs long, and the time for the signal to cross the AO cell is about 67 μs.

Total Number of Calculations

The total number of calculations done during a frame time is $4.3 \cdot 10^{11}$ multiply-and-adds/second. This results from 4 quadrants, 358 μs/frame, 20 pixels/μs, 15,000 pixels (in 75 μs) per IRF, and 1,000 frames/second.

Two tables are presented below. The first table summarizes CCD and AO-cell related properties required by the described architecture. A second table presents several other data architectures with the same 1-KHz frame rate and different signal frequency choices. Note that the maximum number of data samples in an IRF is tabulated along with the number of spare rows on the CCD. This table can also be used if the data rate and frame rate are scaled together.

Parameter	Specification
CCD rows	512
CCD columns	512
Frame rate (Hz)	1,000
AO-cell length (mm)	40
time window (also: transit time) (μs)	67

Table 2. CCD and AO-cell properties.

Option	1	2	3	4	5	6	7	8
f (MHz)	5	5	7.5	7.5	10	10	15	15
μs/line	51.2	51.2	34.1	34.1	25.6	25.6	17.1	17.1
blocks	5	6	8	9	12	14	13	18
IRFs/set	51	42	32	28	21	18	19	14
frame-time (μs)	256	307.2	273.1	307.2	307.2	358.4	221.9	307.2
max IRF duration	177.3	126.1	160.3	126.1	126.1	74.9	211.5	126.1
max data samples/IRF	1773	1261	2404	1892	2522	1498	6344	3784
spare rows	2	8	0	8	8	8	18	8

Table 3. Architectural details corresponding to different input-waveform bandwidths.

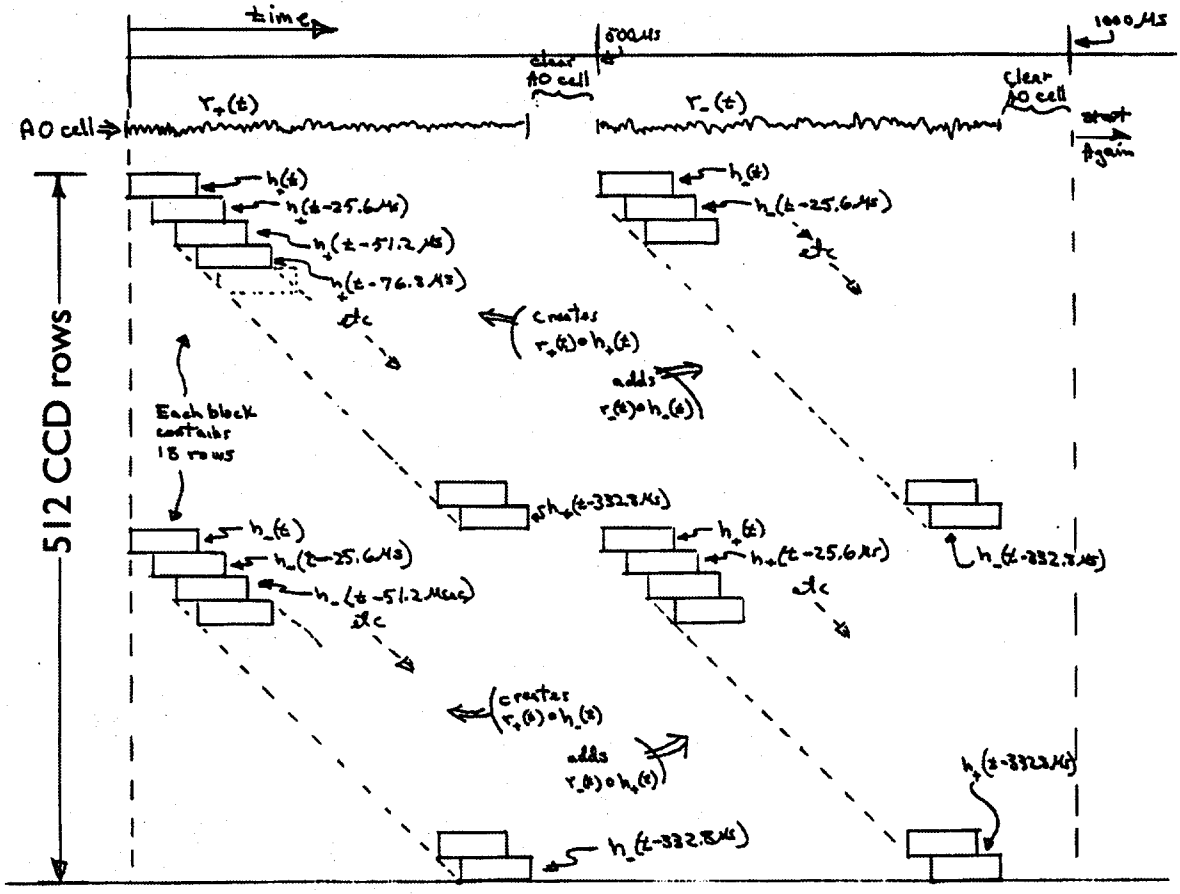

Figure 18. Schematic of proposed optical-correlator architecture.

Optics

A specialized optical preprocessor will require diffraction-limited optics. The specific design can be based on our previous efforts in the case of the Sandia correlator (see Fig. 1 and Ref. 12). Such a nominal design contains an array of laser that are modulated in time according to an ensemble of IRFs, an AO cell, simple optics, and a CCD camera to collect the correlator's output. These nominal components and alternatives are described in the sections below.

Acousto-optic Cells

The capacity of an AO-cell based correlator for parallel processing is ultimately limited by the time-bandwidth product of the cell. This dimensionless product indicates the number of "spots" or parallel optical channels that can be packed into the cell.

Bragg cells can be made with time-bandwidth products on the order of thousands. Shear-mode TeO_2 cells, such as those used in the Sandia correlator, can have time windows up to 100 μs if operated at below 100 MHz. The time-bandwidth product for this material could reach up to 4,000 if the expense and the acoustic non-uniformity of such long cells were acceptable.[10] Future developments in mercurous halide (Hg_2Cl_2) materials may lead to even higher time-bandwidth products. The availability of such devices is currently dependent on improvements in optical quality and fabrication techniques.

Digital Micromirror Devices (DMDs)

An alternative technology received some attention as a replacement for the AO-cell or the sources' array or both. Arrays of micromirrors, developed and produced by Texas Instruments,[6] provide an option for light modulation. Their nominal applications are in video projection and laser printing. Each micromirror can assume one of two positions; effectively *on* and *off*. Unfortunately, the transition time from one position to the other is 20 μs, much too slow to satisfy the architectural requirements described above.[7]

Sources

One of the key elements of the optical correlator described in this report is the array of sources which are modulated in time in accordance with the IRF to be detected in the input signal (see the LED array in Fig. 1). The current solution, LEDs, suffers from slow temporal response and a low radiance level. Two alternatives exist and appear to be on the verge of being practical substitutes for LEDs: vertical-cavity surface-emitting lasers and laser diodes. For future reference, there may be a third alternative; amplified stimulated emission (ASE), currently under development.[8]

A 512-source array called for in the *Architectural Features* section may have to be constructed of several arrays of fewer sources each, potentially utilizing beamsplitters or

mirrors. The main difficulty lies in the expected low yield associated with arrays of more than 128 sources.8 The pitch between sources is also important and should be minimized given the architecture described above. Again, the usage of beamsplitters may assist in achieving this objective. Finally, the sources should require minimal current to operate and exhibit very high power-conversion efficiency at operational settings.

Vertical-Cavity Surface-Emitting Lasers (VCSELs)

Sandia National Laboratories are currently one the premier facilities for VCSEL development and production. These devices can be fabricated in arrays and emit at wavelengths compatible with the rest of the correlator components (687 nm or 850 nm, for example).

Based on *L-I* curve data, VCSELs could be used for grayscale IRF generation.[11] The number of bits would depend on the extent of a monotonically and preferably linearly changing region in the *L-I* data. VCSEL *L-I* curves do not always satisfy these conditions and may exhibit bumps as well as spectral shifts as the drive current is varied and the device shifts from one transverse mode to many.[9]

A figure of merit that is often reported for VCSELs is *wallplug efficiency*. This term must be understood in context: The number reported is derived from a particular current and voltage setting. In the case of grayscale operation, this level of efficiency is unlikely to be maintained over the entire current range.

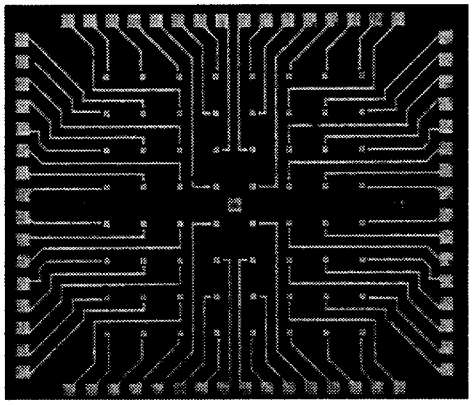

Figure 19. VCSEL array.

VCSEL technology is rapidly evolving, reaching higher power-conversion efficiencies. Before application of these promising sources to the optical correlator discussed here, we must consider the following several questions: (a) how stable is the *L-I* curve, i.e. can a look-up table be constructed to make up for the non-linearity of the relationship?, (b) on what order in time is the jitter between drive-current setting and lasing and how does this number compare to the inverse of the required source bandwidth?, (c) what is the sources' bandwidth measured under conditions resembling actual operation, i.e. accounting for the full range of drive-current?, and (d) how close can the VCSELs be placed, i.e. what is the minimum pitch?

Laser Diodes

Laser-diode arrays represent a more mature technology. Arrays of edge-emitting lasers are available.[8] Laser diodes are a better option for grayscale operation because their *L-I* curves are essentially linear, with a slight deviation around the threshold current.[13,14] Modulation bandwidth of laser diodes is very high (1 GHz) and likely to be limited by packaging-dependent inductances rather than some intrinsic property.

Edge emitters radiate a beam of elliptical cross-section. In most cases, this is an undesirable artifact. In our application, however, if the laser diodes are oriented properly with respect to the AO cell, such a radiation pattern will aid the distribution of light *along* the AO cell.

Conclusions and Further Work

We have shown that correlation-decoding with multiple IRFs is an effective method for bracketing the TEC value encountered by a Dirac-delta-function-like pulse or series of pulses. In that sense, a correlator preprocessor can be an effective attention-focusing device. More accurate TEC values can subsequently be selected by other means within the TEC-range identified by the correlator.

Some of the same correlations carried out by simulation were also performed experimentally using the Sandia AO correlator, previously developed and built at the Laboratories. This correlator had sufficient accuracy so that distinct correlation peaks were obtained in both the grayscale-inputs and binarized-inputs cases. Retention of grayscale information always resulted in a higher-correlation-peak-to-background-fluctuation ratio. Further work is required to determine the optimum number of grayscale bits. By *optimum* we mean a trade-off between immunity to corrupting noises and power consumption and system complexity at the source and AO-cell inputs as well as detector dynamic range. The important advantage of the optical architecture presented here is its inherent capability to perform parallel grayscale multiply-and-adds.

The use of 512 sources, each individually modulated, will require careful consideration of the total power consumed by the sources and the associated digital-to-analog converters (DACs). In short, a comparative study must be performed pitting electronic/digital implementations against the optical architecture outlined in this report in terms of computational speed, power consumption, and complexity. The optical architecture has already been outlined; what remains to be done is a first-order design and analysis of the supporting electronics and a comparison with equivalent all-digital systems.

References

[1]K.T. Stalker, F.M. Dickey, M.L. Yee, B.A. Kast, "Acousto-optic correlator for optical pattern recognition," Ch. 11 in *Real-Time Optical Information Processing*, (Academic Press, 1994), pp. 439-473.

[2]R. Sprague, C.L. Koliopoulos, "Time integrating acousto-optic correlator," *App. Optics*, **15**, No. 1, pp. 89-92, January 1976.

[3]D.Psaltis, "Incoherent electro-optic image correlator," *Opt. Eng.*, **23**, No. 1, pp. 12-15, January/February 1984.

[4]Long waveforms are characteristic of the ionosphere impulse-response problem addressed in this report. This means that a detector element has to integrate for a relatively long time in order to accumulate the complete correlation signal. If this requirement is combined with a large DC signal caused by offsets in the IRFs and the input waveform, unreasonably large well capacities are needed to avoid saturation.

[5]The model used to generate the waveform and IRF data is based on data collectted by *Blackbeard*, an RF-transient measuring package aboard the *Alexis* satellite. *Alexis* which is in low-earth orbit is a DOE developmental system designed by Los Alamos and Sandia National Laboratories. *Blackbeard* records RF transients of up to several hundred microseconds in duration at bandwidths of about 50 MHz. The antennae are two short whips on opposite sides of the vehicle. Triggering is accomplished by simple threshold or time-of-day circuitry. The system has been providing valuable data for almost two years.

[6]Texas Instruments, http://www.ti.com/cgi-bin/pub/search.cgi

[7]C.Tew, L. Hornbeck, *et al.* "Electronic control of a digital micromirror device for projection displays," TA 7.5, *Proceedings of the 1994 IEEE International Solid-state Circuits Conference*, pp. 130-131.

[8]D. Craft, Sandia National Laboratories, private communication, 1995.

[9]M. Hagerott Crawford, R.P. Schneider, Jr., K.D. Choquette, K.L. Lear, "Temperature-dependent characteristics and single-mode performance of AlGaInP-based 670-690-nm vertical-cavity surface-emitting lasers," *IEEE Phot. Tech. Letters*, **7**, No. 7, pp. 724-726, July 1995.

[10]R.B. Brown, J.N. Lee, "Effects of diffraction, scatter, and design on the performance of optical information processors," in *Design Issues in Optical Processing*, ed. J.N. Lee, (Cambridge University Press, 1995), pp. 81-82.

[11]R.P. Schneider, Jr., *et al.*, "Metalorganic vapor phase epitaxial growth of red and infrared vertical-cavity surface-emitting laser diodes," *Jour. of Crystal Growth*, pp. 838-845, 1994.

[12]P.A. Molley, W.C. Sweatt, D.S. Strong, "A miniature acousto-optic image correlator," SPIE 1564, pp. 610-616 (1991).

[13]SDL 1995 Product Catalog, pp. 4-9.

[14]N. Peyghambarian, S. Koch, A. Mysyrowicz, *Introduction to Semiconductor Optics*, (Prentice-Hall, 1993), p. 439.

Distribution:

5	MS	0843	M.L. Yee, 2524
1		0843	K.T. Stalker, 2524
2		0970	J.R. Kelsey, 5700
1		0972	A.J. Medina, 5722
5		0980	M.R. Descour, 5725
5		0980	W.C. Sweatt, 5725
5		0980	G.R. Elliott, 5725
1		0980	S.M. Gentry, 5725
1		0980	C.A. Boye, 5725
2		0978	R.E. Spalding, 5909
1		9018	Central Tech Files, 8523-2
5		0899	Technical Library, 4414
2		0619	Review and Approval Desk, 12630 For DOE/OSTI